

Numerical Approach Aspects for the Investigation of the Longitudinal Static Stability of a Transport Aircraft with Circulation Control

Dennis Keller

Abstract The aim of the investigation is to gain more certainty about the approach to evaluate the longitudinal stability and controllability of a high-lift configuration of a transport aircraft with circulation control. Since the work was carried out with a CFD RANS approach, a comprehensive meshing study was performed in advance.

1 Introduction

In compliance with the vision *Flightpath 2050*, the German research project *SFB 880* is investigating a STOL aircraft configuration, which possibly allows to reduce emissions and travel time by utilizing existing aerospace infrastructure more efficiently. In order to achieve short runway usage, an active high-lift system in terms of circulation control (CC) is employed. The potential of such systems is already well known (see [5, 8]) and is further assessed within the research project by M. Burnazzi [2]. However, the technology raises new questions, which are not adequately addressed so far. One of those is how CC will impact the handling qualities of a transport aircraft. For example, it is expected that the high flap loading and the low dynamic pressure during take off and landing will pose challenges to the flight control systems. This paper gives an aerodynamic view of the longitudinal static stability issue by investigating the flight mechanical properties of a circulation controlled wing itself, its influence on the HTP and eventually of the whole aircraft. Prior to the analysis, a meshing study was performed on a simplified 2D geometry in order to derive an efficient and accurate meshing strategy for the 3D configuration.

D. Keller (✉)

Institute of Aerodynamics and Flow Technology, German Aerospace Center,
38108 Braunschweig, Germany
e-mail: Dennis.Keller@dlr.de

Table 1 Number of grid points

	Coarse	Medium	Fine
Structured	128454	524558	2119854
Hybrid_PW	–	284918	–
Hybrid	84856	181714	337342

2 Flow Solver

The calculations are performed with the *DLR TAU* code [6], which is based on an unstructured finite volume approach for solving the Reynolds-averaged Navier Stokes equations. For this investigation, the implicit LUSGS scheme is used for time stepping and a central scheme for the spatial discretization of the convective fluxes. The turbulence effects are modeled with the original Spalart-Allmaras formulation (SA) [12] with vortical and rotational flow correction based on the Spalart-Shur correction [13].

3 Test Configurations

3.1 2D Configuration

The 2D geometry represents a cut through the wing of the reference aircraft at the location of its mean aerodynamic chord. In order to investigate discretization influences especially near the active flow outlet, several cell size settings as well as different meshing methods were utilized (Table 1). Hybrid meshes were created with Pointwise [10] (Hybrid_PW) and Centaur [3] (Hybrid), whereas structured meshes were solely built with the former (Structured) (Fig. 1). The edge lengths along the surface were kept almost equal within the refinement levels. However, small adaptations had to be introduced on the Centaur meshes in order to achieve an optimal boundary layer discretization. Furthermore, in contrast to the structured meshes, the wall distances of the quad layers were kept constant on these meshes.

3.2 3D Configuration

At the beginning of the *SFB 880* research project, an aircraft with a capacity of 100 passengers was designed with the preliminary aircraft design tool *PrADO* [7]. The wing's span measures 28.8 m with an aspect ratio of 9 and a leading edge sweep of 10°. The HTP's span equals 10.4 m, resulting in a relative tail volume of 1.235. The underlying 3D geometry (Fig. 5) represents the landing configuration of this design,

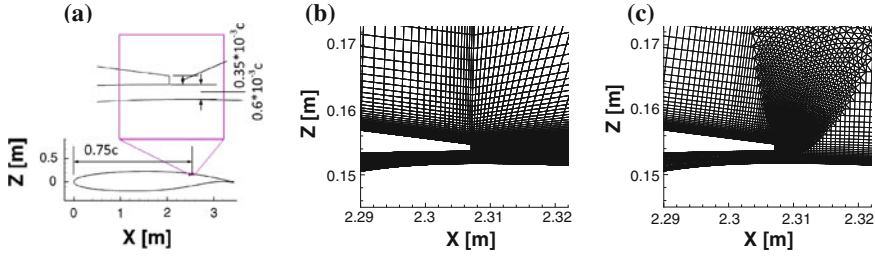


Fig. 1 Slot region. **a** Geometry. **b** Structured mesh. **c** Hybrid mesh

which has no leading edge device but a circulation controlled plain flap and aileron with 65° deflection and 45° droop, respectively. Hybrid meshes were built for the tail-off configuration and for the whole aircraft based on the experiences from the 2D investigations. The wing wake was refined with either tetrahedra or with a structured hexahedron box. A modular mesh approach was chosen in order to trim the aircraft with the smallest possible meshing influence.

4 Computational Results

4.1 Preliminary 2D Studies

Grid Convergence Study When working with complex geometries, semi automated hybrid mesh generators often seem to be the best choice as they offer a good compromise between work effort and quality of results. However, the quality may become unacceptable low when the automated mesh topology does not reflect the flow topology. Typical examples for this are free shear layers. With the investigation of wake interaction and CC in general, these types of flow phenomena are of particular importance. Therefore, the main purpose of the meshing study was to evaluate the feasibility of using a semi automated hybrid mesh generator for these kind of problems. Furthermore, a grid convergence study was carried out for both the structured as well as the hybrid mesh approach.

Figure 2 shows the influence of the grid resolution on the global coefficients for both mesh families. While the coefficients of the structured mesh show a clear trend, the hybrid meshes have a change in gradients at the medium size mesh. However, when considering the difference in grid sizes, the hybrid meshes deliver good results. Following G. de Vahl Davis [4] and applying the Richardson Extrapolation on the structured mesh family, the *exact* coefficients and the deviations of the medium sized meshes can be derived [11]. With far less than one per cent in deviation from the *exact* lift and moment coefficients, both medium size meshes show excellent results (Table 2). The comparably high difference in drag is probably coming from small

Fig. 2 Grid dependence of global coefficients

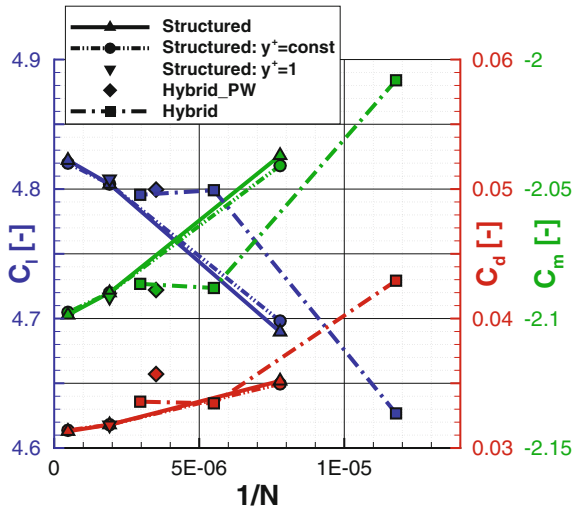


Table 2 Error estimates for global coefficients

	Coarse		Medium			Fine	
	Structured	Hybrid	Structured	Hybrid_PW	Hybrid	Structured	Hybrid
$\frac{c_l - c_{l,R.ex.}}{c_{l,R.ex.}} [\%]$	2.82	4.12	0.455	0.54	0.56	0.073	0.625
$\frac{c_d - c_{d,R.ex.}}{c_{d,R.ex.}} [\%]$	12.77	37.58	1.93	14.46	7.12	0.31	7.63
$\frac{c_m - c_{m,R.ex.}}{c_{m,R.ex.}} [\%]$	3.01	4.39	0.488	0.54	0.57	0.079	0.65

pressure differences on the flap, which have a large influence on the drag coefficient due to its order of magnitude.

The pressure distribution supports this assumption (Fig. 3). While showing only slight differences in most parts, the suction peak on the coanda surface indicates a bigger impact by the discretization level. It also reflects the change in gradients of the global coefficients of the hybrid mesh family, with the peak being stronger on the medium hybrid mesh than the one on the fine hybrid mesh.

The velocity profiles within the boundary layer show a fairly good agreement for the medium and fine meshes in all investigated cuts except at the slot exit (Fig. 4). Here, the velocity within the slot seems to be overestimated on all hybrid Centaur meshes. Furthermore, the velocity distributions on the coarse and the medium hybrid mesh show a peak towards the upper wing surface. Comparison to experimental investigations of circulation controlled airfoils [1, 9] lead to the assumption, that these peaks are unphysical and arise due to the O-type topology at the wing trailing edge. In contrast, the velocity profiles on all structured meshes show a homogeneous distribution. However, the higher velocities at the slot exit on the hybrid meshes do not seem to have a big influence on the general flow topology, since this difference cannot be detected in the velocity distributions further downstream anymore.

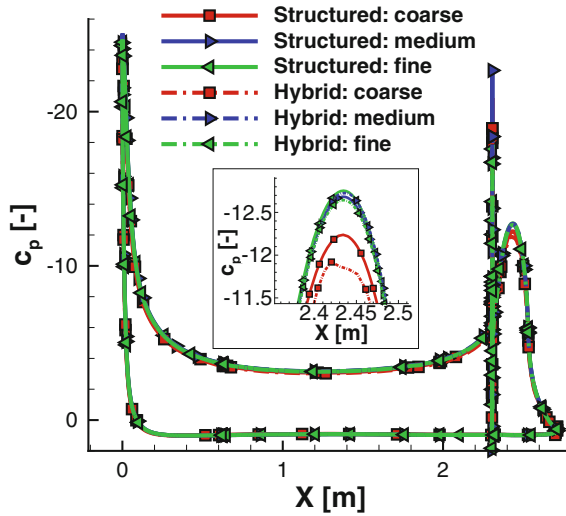
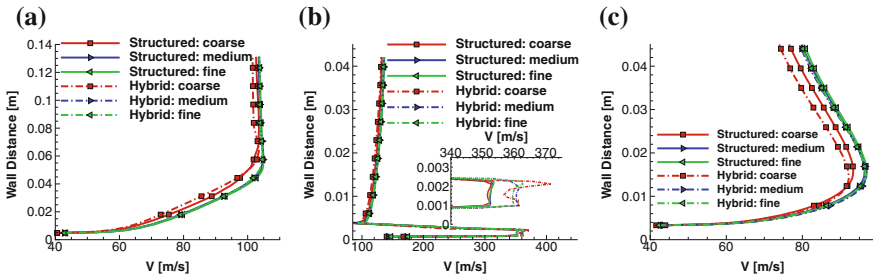


Fig. 3 Pressure distribution

Fig. 4 Velocity profiles in boundary layer along the upper surface. **a** $x/c=0.45$. **b** $x/c=0.75$. **c** $x/c=0.84$

4.2 3D Configuration

Wake Meshing Influence For the investigation of the longitudinal handling qualities, the HTP's efficiency is of particular importance. It is driven by downwash effects and altered dynamic pressure due to the wake of the main wing. The former is visualized for a cutting plane through the basic mesh at the leading edge of the HTP's mean aerodynamic chord (Fig. 5) in Fig. 6. The velocity vectors confirm the existence of an inboard flap vortex and a wing tip vortex. Between these vortices, the vertical velocity reaches about 30 % of the free stream velocity. When enhancing the wake resolution by halving the edge length of the tetrahedra, the contour of the vortices sharpens. Besides the increased strength of the vortical flow around the vortex cores, the delta plot of the local angle of attack also reveals two merging vortex cores in the outboard region instead of one (Fig. 7a).

Fig. 5 Vortex visualization and position of cutting plane on the tetrahedral refined mesh

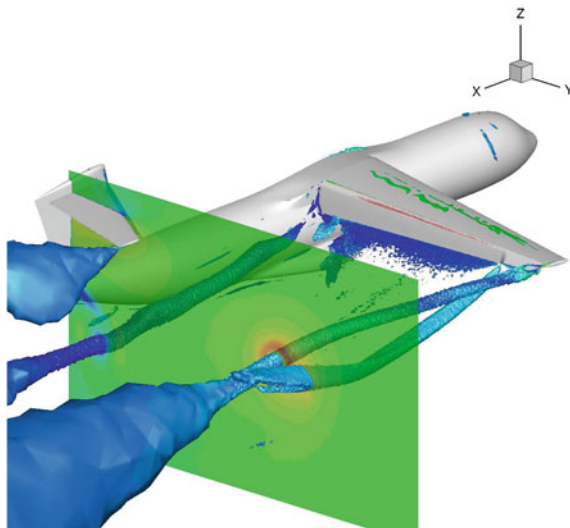
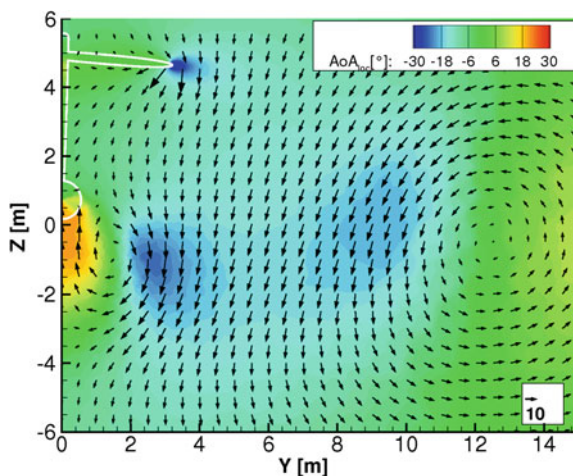


Fig. 6 Flow characteristics on basic mesh in x-plane at $x = 29.4$ m



Regarding the outboard vortex system, the trend is even more visible on the mesh with hexahedral wake refinement (Fig. 7b). However, the plot shows a rather clustered picture of the inboard flap vortex, which leads to the assumption that the transition between structured and unstructured elements behind the origin of the inboard flap vortex is negatively affecting the vortex resolution.

Downwash Investigation When employing CC on a flap, one can distinguish between two different operating modes. For comparably low blowing coefficients, the flow on the flaps is not completely attached and the energization regulates the amount of separation. This utilization is called boundary layer control and is the

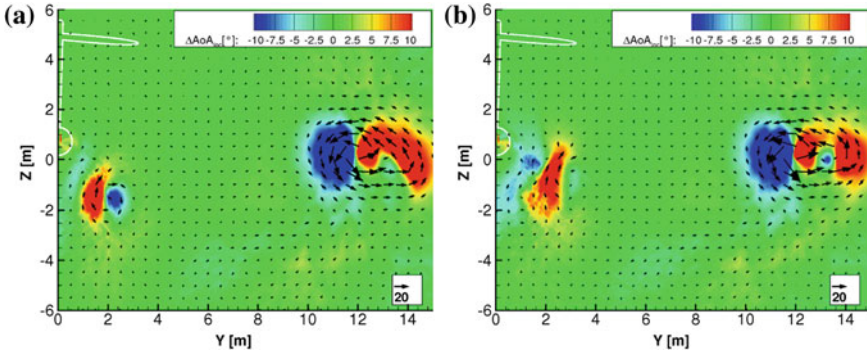


Fig. 7 Delta of local angle of attack in x-plane at $x = 29.4$ m. **a** Difference plot between tetrahedral refinement and basic mesh. **b** Difference plot between hexahedral refinement and basic mesh

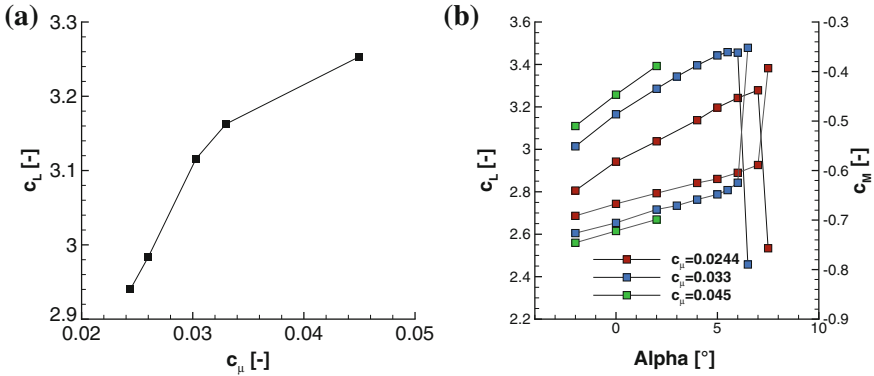


Fig. 8 Lift coefficients of wing-body configuration. **a** Lift coefficients at $\alpha = 0^\circ$ for different blowing coefficients c_μ . **b** Lift and pitching moment at the aerodynamics center over α

most effective way to use CC. After reaching fully attached flaps, additional blowing leads to so-called super-circulation, which is less effective. For landing cases, the threshold between these two utilization ranges is interesting, as it gives the maximum lift at good effectiveness. The investigation was conducted at three global blowing coefficients which reflect these characteristics (Fig. 8). These coefficients result from an optimized pressure setting in each of six different plena along the span (Fig. 10b). Figure 9a shows the downwash along the position of the quarter chord line of the HTP for the chosen blowing settings at $\alpha = 0^\circ$. As expected, the downwash increases with increasing blowing coefficient. Furthermore, the local angle of attack dips in spanwise direction. The slightly different gradient at the lowest blowing ratio is due to an altered wing loading. Figure 9b compares the change of downwash due to a change in lift caused by an altered angle of attack on the one hand and a modified blowing coefficient on the other. It shows that the values of the gradients are lower and constant for lift increases due to changed blowing. The gradients for constant

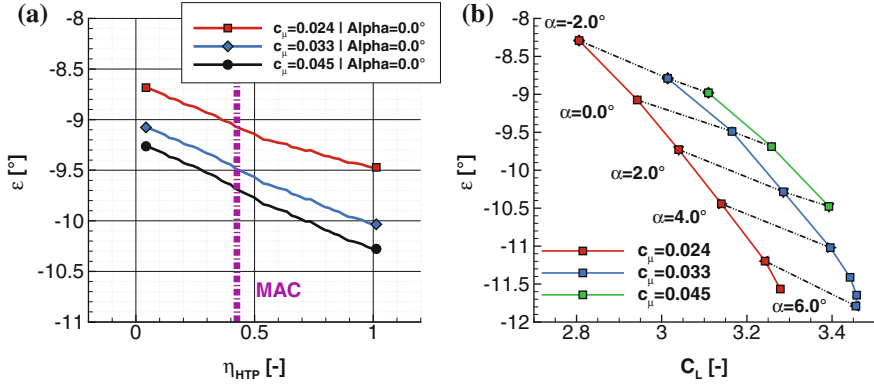


Fig. 9 Downwash at the horizontal tail plane position. **a** Downwash at $\alpha = 0^\circ$ along HTP span. **b** Change of downwash due to change in lift coefficient

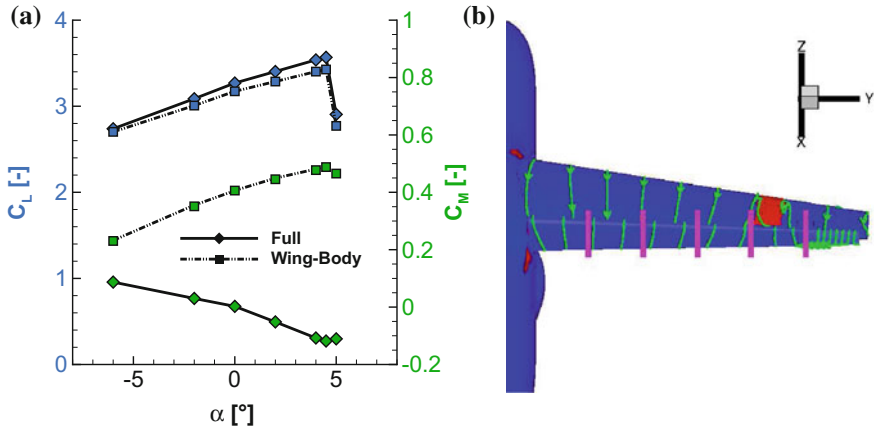


Fig. 10 Aerodynamic characteristics of trimmed landing configuration. **a** Global coefficients over angle of attack α for $i_{HTP} = 16.13^\circ$. **b** Separation behavior and plena positions

blowing get slightly steeper towards higher angle of attacks due to the reduced distance between the main wing wake and the HTP position. The break down near α_{\max} is associated with a shift in the main wing loading and a resulting change in downwash distribution.

Static Stability Investigation The preliminary aircraft design led to a maximum rearward position of the center of gravity, which has to be confirmed. The CFD simulations of the landing configuration show the aerodynamical feasibility, even though the maximum trim angle of the horizontal stabilizer from the preliminary design is exceeded by around 8° . Figure 10a shows that with a trim angle of $i_{HTP} = 16.13^\circ$ the configuration is still controllable at an angle of attack of $\alpha = 0.0^\circ$. Below α_{\max} it is also stable while satisfying the stability reserve requirement with

$\Delta x_{S25}/l_\mu \approx -0.15$. However, there is a high risk, that the configuration is not stable during stall due to its outboard stall mechanism (Fig. 10b) and the resulting additional downwash at the HTP. In this context it is worth mentioning that the wing itself has a nose down tendency after α_{\max} .

5 Summary

The preliminary 2D studies justify the meshing approach, especially the usage of hybrid meshes, for the 3D calculations. Even though embedding a structured hex box into an unstructured mesh region most likely leads to a more efficient way to resolve wake characteristics, the interface regions between these two cell types can lead to higher discretization errors resulting in unexpected vortex distortions. The high lift values obtained by circulation controlled configurations lead to a strong downwash behind the main wing, which is dependant not only on the lift coefficient itself but also on the way the lift is created. Even though the CFD results confirm the feasibility of the most rearward position of the center of gravity from the preliminary design, the necessary HTP trim angles are exceptionally high due to the downwash. Furthermore the results of the post stall simulation, which have to be treated with caution, lead to the assumption that the wing design and its associated stall mechanism are unfavorable regarding the longitudinal handling qualities and result in unstable flight conditions.

References

1. Allan, B.G., Jones, G.S., Lin, J.C.: Reynolds-averaged navier-stokes simulation of a 2D circulation control wind tunnel experiment. AIAA Paper 2011-25 (2011)
2. Burnazzi, M., Radespiel, R., Keller, D.: Numerical simulation of a 3D aircraft model equipped with active Coanda high-lift devices. 18. DGLR-Fach-Symposium der STAB, Stuttgart, Germany (2012).
3. CentaurSoft: <http://www.centaursoft.com> (2012). Accessed on June 2012
4. de Vahl Davis, G.: Natural convection of air in a square cavity: a benchmark numerical solution. Int. J. Numer. Meth. Fluids. **3**(3), 249–264 (1983)
5. Englar, R.J., Blaylock, G.M., Gaeta, R.J.: Recent experimental development of circulation control airfoils and pneumatic powered-lift systems. AIAA Paper 2010–345 (2010)
6. Gerhold, T.: Overview of the Hybrid RANS Code TAU. Notes on Numerical Fluid Mechanics and Multidisciplinary Design, vol. 89, pp. 81–92 (2005)
7. Heinze, W., Österheld, C.M., Horst, P.: Multidisziplinäres Flugzeugentwurfsverfahren PrADO - Programmwurf und Anwendung im Rahmen von Flugzeug-Konzeptstudien. Vortrag DGLR-2001-194, DLR-Jahrestagung 2001 in Hamburg, erschienen im DGLR-Jahrbuch 2001, Band 3, S.1701-1712, DGLR, Bonn (2001)
8. Korbacher, G.K.: Aerodynamics of powered high-lift systems. Annu. Rev. Fluid Mech. **6**, 319–358 (1974)
9. Pfingsten, K.-C., Jensch, C., Körber, K.W., Radespiel, R.: Numerical Simulation of the Flow around Circulation Control Airfoils. First CEAS European Air and Space Conference, Berlin, Germany (2007)

10. Pointwise: <http://www.pointwise.com> (2012). Accessed on June 2012
11. Roache, P.J.: Quantification of uncertainty in computational fluid dynamics. *Annu. Rev. Fluid Mech.* **29**, 123–160 (1997)
12. Spalart, P.R., Allmaras, S.R.: A one-equation turbulence model for aerodynamic-flows. *AIAA Paper* 92–0439 (1992)
13. Spalart, P.R., Shur, M.: On the sensitization of turbulence models to rotation and curvature. *Aerosp. Sci. Technol.* **1**(5), 297–302 (1997)

New Results in Numerical and Experimental Fluid
Mechanics IX

Contributions to the 18th STAB/DGLR Symposium,
Stuttgart, Germany, 2012

Dillmann, A.; Heller, G.; Krämer, E.; Kreplin, H.-P.;
Nitsche, W.; Rist, U. (Eds.)

2014, XVI, 683 p. 427 illus., 105 illus. in color.,
Hardcover

ISBN: 978-3-319-03157-6